The ZEPLIN-III dark matter detector: performance study using an end-to-end simulation tool

H. M. Araújo [a,b,*], D. Yu. Akimov [c], G. J. Alner [b], A. Bewick [a],
C. Bungau [b], B. Camanzi [b], M. J. Carson [e], V. Chepel [d],
H. Chagani [e], D. Davidge [a], J. C. Davies [e], E. Daw [e],
J. Dawson [a], T. Durkin [b], B. Edwards [a,b], T. Gamble [e],
C. Ghag [f], R. Hollingworth [e], A. S. Howard [a], W. G. Jones [a],
M. Joshi [a], J. Kirkpatrick [e], A. Kovalenko [c],
V. A. Kudryavtsev [e], V. N. Lebedenko [a], T. Lawson [e],
J. D. Lewin [b], P. Lightfoot [e], A. Lindote [d], I. Liubarsky [a],
M. I. Lopes [d], R. Lüscher [b], P. Majewski [e], K. Mavrokoridis [e],
J. McMillan [e], B. Morgan [e], D. Muna [e], A. S. Murphy [f],
F. Neves [d], G. Nicklin [e], S. Paling [e], J. Pinto da Cunha [d],
R. Preece [b], J. J. Quenby [a], M. Robinson [e], C. Silva [d],
V. N. Solovov [d], N. J. T. Smith [b], P. F. Smith [b],
N. J. C. Spooner [e], V. Stekhanov [c], T. J. Sumner [a],
D. R. Tovey [e], C. Thorne [a], E. Tziaferi [e] & R. J. Walker [a]

[a]*Blackett Laboratory, Imperial College London, UK*

[b]*Particle Physics Department, Rutherford Appleton Laboratory, Chilton, UK*

[c]*Institute for Theoretical and Experimental Physics, Moscow, Russia*

[d]*LIP–Coimbra & Department of Physics, University of Coimbra, Portugal*

[e]*Department of Physics & Astronomy, University of Sheffield, UK*

[f]*Department of Physics & Astronomy, University of Edinburgh, UK*

Abstract

We present results from a GEANT4-based Monte Carlo tool for end-to-end simulations of the ZEPLIN-III dark matter experiment. ZEPLIN-III is a two-phase detector which measures both the scintillation light and the ionisation charge generated in liquid xenon by interacting particles and radiation. The software models the instrument response to radioactive backgrounds and calibration sources, including the generation, ray-tracing and detection of the primary and secondary scintillations in liquid and gaseous xenon, and subsequent processing by data acquisition electronics. A flexible user interface allows easy modification of detector parameters at run time. Realistic datasets can be produced to help with data analysis, an example of which is the position reconstruction algorithm developed from simulated data. We present a range of simulation results confirming the original design sensitivity of a few times 10^{-8} pb to the WIMP-nucleon cross-section.

1 Introduction

ZEPLIN-III is a two-phase (liquid/gas) xenon detector developed by the UK Dark Matter Collaboration and international partners,[1] which will try to identify and measure galactic dark matter in the form of Weakly Interacting Massive Particles, or WIMPs [1,2]. Upon completion of physics testing now underway at Imperial College London, the system may join the ZEPLIN-II [3] and DRIFT-IIa [4] experiments already operating 1100 m underground in our laboratory at the Boulby mine (North Yorkshire, UK).

Two-phase emission detectors based on the noble gases date back several decades [5], but this technology has gained momentum since the ZEPLIN Collaboration first explored the potential of high-field xenon systems [6,7,8]. The operating principle is that different particle species generate different amounts of scintillation light and ionisation charge in liquid xenon (LXe). The ratio between these two signal channels provides a powerful technique to discriminate

* Corresponding author; address: Astrophysics Group, Blackett Laboratory, Imperial College London, SW7 2BW, UK
   Email address: H.Araujo@imperial.ac.uk (H. M. Araújo).
[1] Edinburgh University, Imperial College London, ITEP-Moscow, LIP-Coimbra, Rutherford Appleton Laboratory and Sheffield University.

between electron and nuclear recoil interactions. WIMPs are expected to scatter elastically off Xe atoms, much like neutrons, and the recoiling nucleus will produce a different signature to γ-ray interactions and other sources of electron recoils.

WIMP detectors differ from more traditional detectors of nuclear radiation in that they require: i) extremely low radioactive and cosmic-ray backgrounds, addressed by the use of radio-pure materials and operation deep underground; ii) excellent discrimination of the remaining background events, hopefully better than 1000:1 rejection efficiency for electron recoils; iii) a low energy threshold for nuclear recoils, since the kinematics of WIMP-nucleus scattering results in a very soft recoil spectrum ($\lesssim$100 keV).

Monte Carlo simulations are essential in these key areas. Acceptable levels of trace contamination must be assessed for all detector materials, requiring simulations of internal and external backgrounds expected from each component. Cosmic-ray-induced backgrounds also need careful calculation, since experimental measurements would require nothing short of a dedicated WIMP detector. Having established the residual electron/photon and neutron event rates, the level of discrimination and energy threshold which can realistically be achieved must be calculated with the help of detailed detector simulations – and possibly fed back to the design process. In addition, the data produced by two-phase detectors are often complex, and particular simulations are required to help extract actual physics parameters. Finally, realistic datasets help with planning the data acquisition electronics and the data analysis software.

In this paper we describe a simulation tool used throughout this process [9], based on the GEANT4 Monte Carlo toolkit [10]. The package builds upon previous simulation work [11,12,13] and experimental measurements with high-field, two-phase prototype detectors [7,8]. After overviewing the detector and the software, a description is given of the simulation models used to calculate the detector response. Simulation results are then presented for the dominant background contributions, calibration runs with γ and neutron sources, and position reconstruction capabilities, leading to a predicted performance of the instrument as a WIMP detector.

1.1 The ZEPLIN-III detector

The WIMP target is housed in a 1-m tall vacuum cryostat, which contains a xenon vessel sitting on top of a liquid nitrogen reservoir. The latter cools the xenon chamber to around -100°C. All major metal components of the detector are made from high-purity C101 copper. Inside the xenon vessel an array of 31 2-inch photomultiplier tubes (PMTs) is immersed in the liquid phase,

looking up to a $\simeq$40-mm thick LXe disk topped by a 5-mm layer of gas. Up to 40 kV can be applied between a polished copper plate covering the gas phase (hereafter 'anode mirror') and a metal wire grid located 35 mm below the liquid surface ('cathode grid'), defining the active region of the detector. A second wire grid ('PMT grid') placed just above the array (5 mm below the cathode) defines a reverse field region which suppresses secondary signals from low-energy photons from the PMTs and helps protect the PMT photo-cathodes from stray electric fields. The PMTs, arranged in a closely-packed hexagonal array, are encased in 2-inch holes bored in a copper screen in order to prevent optical cross-talk. A lower plate ('PMT mirror') covers the array; this mirror has conical cuts around the PMT windows intended to improve the light collection and prevent the escape of stray light generated around the PMT bodies. The diameter of the active LXe volume is approximately 40 cm, while that of the PMT array is 34 cm. The array is powered by a network of thin copper plates located inside the xenon vessel, which provides common connection to each dynode on all the PMTs and hence reduces the number of required feedthroughs quite considerably. A detailed description of the detector construction is given elsewhere [14]. We refer to Fig. 1 for the model representation of the ZEPLIN-III geometry.

When a particle interacts in LXe, VUV scintillation light is promptly produced. In addition, a strong electric field (up to ~ 8 kV/cm) prevents most of the ionisation charge produced around the particle track from recombining. The extracted charge carriers drift upward to the liquid surface, and are emitted into the gas phase. Here, the strong electric field (double that of the liquid phase) leads to the production of further VUV photons, by the process known as electroluminescence or proportional scintillation. Therefore, both scintillation and ionisation signals give rise to optical signatures which are detected with the same PMT array, the time separation between them being proportional to the vertical (z) coordinate. We label these signals as the 'primary' and the 'secondary', or S1 and S2, respectively. The ratio S2/S1 is higher for electrons than nuclear recoils. In low-energy atom-atom collisions, most of the energy loss goes into recoil of the nuclei and only a small fraction converts into electronic loss (i.e. electron excitation/ionisation). Electron/γ-ray interactions act directly on the outer atomic electrons, yielding more ionisation charge.

The 31 PMT signals are fed into wideband amplifiers and split into a dual-range data acquisition system (DAQ). A large dynamic range ensures sensitivity to very small primaries containing only a few photoelectrons (phe) as well as large secondaries without saturation. All 62 channels are sampled at 500 MS/s by 8-bit digitisers.

The main requirements underlying the software design were: i) that it should model the transport and interactions of particles internal and external to the detector, down to the production of electron and nuclear recoils; ii) simulate the physical processes involved in the generation of the optical response to scintillation and electroluminescence; iii) generate the electrical response (digitised voltage timelines) for all channels in order to produce realistic datasets; iv) operating parameters should be easily modified by the user, in particular the LXe height and the applied electric field; v) it should be user friendly.

GEANT4 is arguably the most comprehensive toolkit of its kind, and the only one to fulfil the above requirements. Besides an extensive list of physics models, its modular and transparent design means that new ones can be easily added (e.g. electroluminescence). Its flexibility allows further processing of simulated events (DAQ, event display, data analysis, etc.). Versatile specification of the primary particle generator means that individual particles, radioisotopes and sources with complex spatial and energy distributions can be specified at run time. Finally, user-interfaces are easily created, allowing the user to control most physics parameters without having to delve into the code itself. This is important since many optical and charge transport properties are still ill-defined, and different parameter combinations have to be assessed. In this package, primary generator, detector and physics parameters can be set interactively by commands and macros available for many simulation tasks.

2   The simulation model

2.1   GEANT4 solid model

Two geometry representations have been set up. The one shown in Fig. 1 includes most detector components located above the liquid nitrogen vessel. A second geometry implements only the (optically) active region, comprised between the PMT photocathodes and the anode mirror. Less computationally demanding than the full model, this is useful for light collection and similar studies. Both produce exactly the same optical response. The LXe height, chosen by default to be 35 mm above the cathode (leaving 5 mm of gas below the anode mirror) can also be set between runs. This entails modifying the electric field distribution as well as optical and other properties, as explained below. Additional external components will be included at a future stage, namely a scintillator veto system surrounding the detector as well as hydrocarbon and lead shielding for external neutrons and γ-rays, respectively.
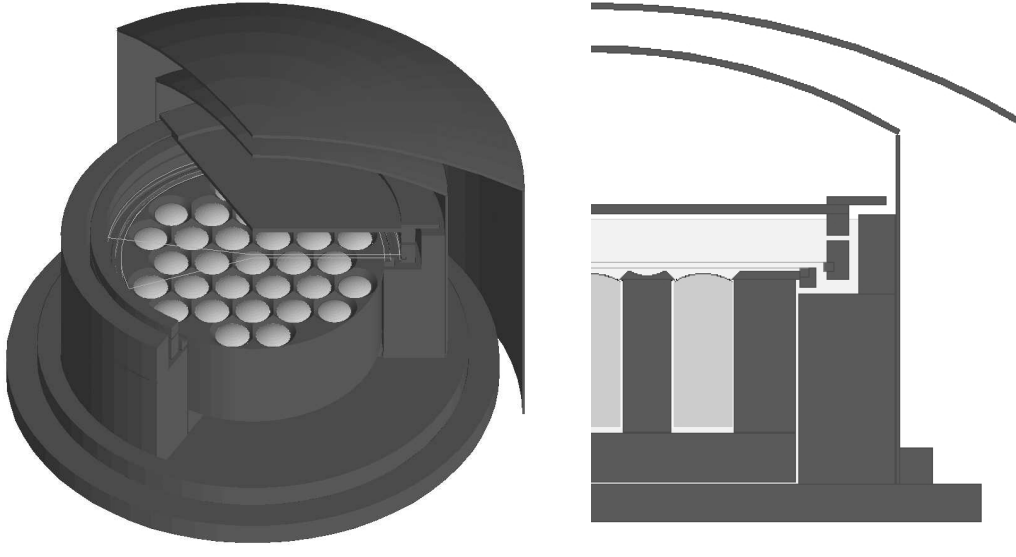
Fig. 1. Cut-out (left) and cross-sectional (right) views of the GEANT4 implementation of the 'full' ZEPLIN-III geometry.

2.2 The optical model

Optical ray-tracing in the detector takes into account the optical constants of liquid and gaseous xenon, the angular reflectivities of copper surfaces and electrode grids, and the optical and detection properties of the PMTs, all of which are defined at the xenon scintillation wavelength of $\sim$175 nm (7 eV).

For LXe a refractive index n=1.69 and an attenuation length of 36.4 cm were considered [15]. Although the latter is probably dominated by Rayleigh scattering (c.f. Ref. [16], as well as preliminary results from our ZEPLIN-II detector), only photo-absorption was considered here – the difference in light collection is relatively small.

The angular reflectivity of copper is quite uncertain at VUV wavelengths, depending on the surface finish, oxidation state and possible LXe condensation onto the cold surfaces. A single measurement was found, indicating R=25% for normal incidence for a clean-cut surface [17]; a more conservative 15% was adopted instead. The GEANT4 'unified' model [18] was chosen to treat the angular reflection from metal surfaces; the parameter σ_α, which characterises the Gaussian smearing of the exit angle in this model, was set to 20º, producing a half-width $\approx$45º for normal incidence. We point out that the choice of model is not informed by experimental data – lacking for many materials for this wavelength range. A high-reflectivity case (R=90% for anode and PMT mirrors) was also considered, to assess the benefit of electroplating the mirrors in a future upgrade.

6

The two electrode grids (wire-wound) are implemented as continuous dielectric sheets with refractive index matched to that of LXe (no Fresnel reflection) but with an absorption length chosen to give 10% absorption at normal incidence (equal to the grid wire/pitch ratio). The dielectric absorption mimics the obscuration of light with angle of incidence to good approximation for all but the largest angles with respect to the grid normal.

The PMT models consider a curved quartz window supporting an opaque photocathode with a user-defined quantum efficiency (QE). A photon is detected as a photoelectron depending on the outcome of a random throw. Note that manufacture-quoted QEs are usually measured in air or vacuum. A slightly better optical match is obtained when PMTs are immersed in LXe due to the similar refractive indices (n=1.6 for quartz). However, given that other losses are also considered (e.g. window absorption and reflection from metal fingers deposited onto it for improved low-temperature performance), we can assign the measured PMT QE to the photocathode without major error. Low-temperature QEs average 30% for xenon scintillation for the ZEPLIN-III phototubes [19].
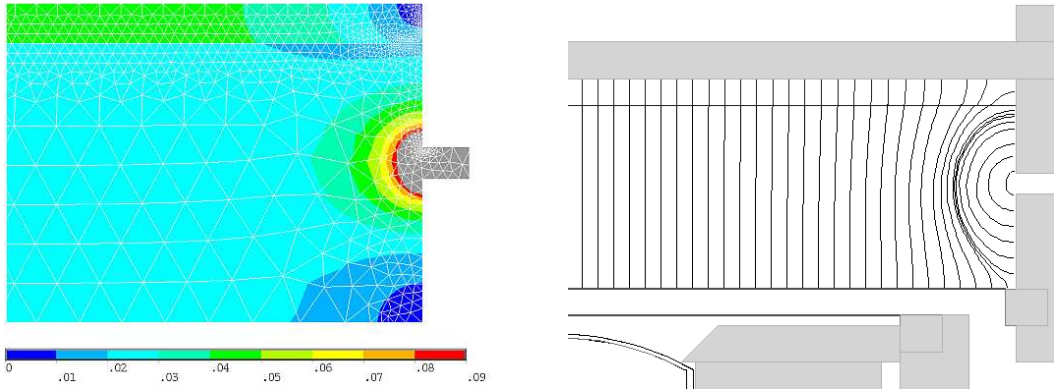
2.3 Electric fields

Fig. 2. Left: ANSYS [20] electric field contour map and optimised meshing in peripheral regions of the detector. Right: Simulated trajectories for charge released at the cathode grid and side electrode.

The flat, disk-shaped LXe target ensures uniform electric fields (and light collection) above the PMT array. Inside this central ('fiducial') volume, high discrimination efficiency should be achieved. Interactions in outlying regions, which can probe non-vertical fringe fields, may still be corrected (or rejected) by use of 3-dimensional event information. To ensure that this procedure is well understood, the simulation uses detailed electric field models for both phases. This is particularly important for the electroluminescence signal: the field determines not only how much ionisation is extracted from the interaction

site, but also its drift time to the surface, the emission probability and location, the electroluminescence yield in the gas and the temporal development of the signal.

Two-dimensional electric field maps are used by the electroluminescence model; by exploiting the cylindrical symmetry of the target, these maps can be kept small and are easily navigated. The standard GEANT4 tracking kernel is applied to all other particles, so there is no penalty to other processes. The ANSYS [20] finite-element software was used to produce field maps for several gas gaps, for a reference voltage of 1 V between the anode mirror and the cathode grid. The reverse-field region below the cathode grid, which suppresses S2 signals from low-energy PMT photons, is not implemented. Dielectric constants for the gas and liquid phases are ϵ_g=1 and ϵ_l=2, respectively. The total inter-electrode voltage (set interactively) scales the chosen field map to obtain the correct electric field strength. Fig. 2 (left) represents the ANSYS contour plot and the optimised meshing for the default map (5 mm gas). Electron trajectories obtained with a simple field navigation are shown in Fig. 2 (right). Note that the field is constant above the array, well away from the edge.
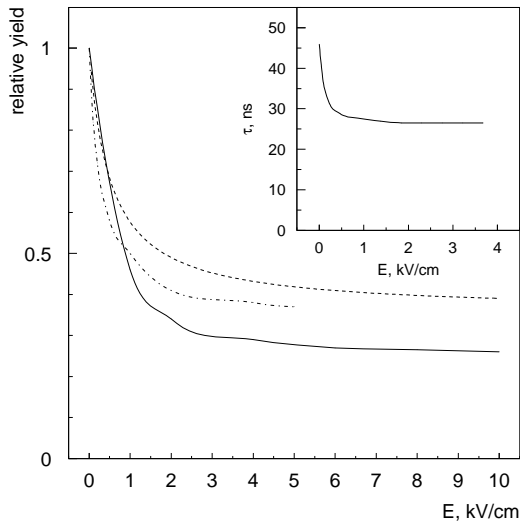
2.4   The primary signal

Fig. 3. Electric-field dependence of the scintillation yield for 1 MeV electrons [23] (continuous line), ∼200 keV Compton electrons [29] (dashed) and 122 keV γ-rays [28] (dash-dot). The inset shows the decay time constant (pulse area/amplitude) for ∼200 keV Compton electrons [29].

As a scintillator LXe compares favourably with the best crystals, yielding some 60 photons per keV of energy deposited (electron equivalent, hereafter 'keVee') [21,22]. The VUV luminescence is produced by the decay of singlet

and triplet states of the Xe_2^* excimer. These can be excited directly by the interacting particle or as a result of recombination along the particle track ($Xe_2^+ + e^- \rightarrow Xe_2^*$)[23,24]. Recombination is very efficient for nuclear recoil interactions, and so their scintillation is faster ($\tau \simeq 21$ ns in a single-exponential approximation) than for electrons ($\tau \lesssim 45$ ns, depending on energy) [23,25]. This discrimination technique was exploited in the ZEPLIN-I detector [26].

The scintillation efficiency for nuclear recoils is lower than for electron interactions of the same energy. A zero-field quenching factor QF=0.22 [25] was used in the simulation regardless of energy. Very recent data agree with this value at a few tens of keV (nuclear-recoil energy, 'keVnr'), but may indicate some reduction at lower energies [27,28].

An external electric field suppresses recombination to a varying degree, affecting mainly the light yield and decay times for electron recoils, as depicted in Fig. 3. The scintillation model (adapted from that implemented in GEANT4) assumes a uniform electric field across both phases, i.e. yields and time constants are position-independent. This is not unreasonable considering that, for the range of interesting fields, these properties do not vary appreciably. The default yields for electron and nuclear recoils were set at 18 photons/keV and 12 photons/keV, respectively, at the nominal 8 kV/cm field. The number of VUV photons is Gaussian-distributed (except when fewer than 10, in which case Poisson deviates are used), with unity Fano factor – note that for relatively small S1 the overall energy resolution is instead dominated by photoelectron statistics. Although pulse-shape analysis of S1 cannot provide as good a discrimination as in a zero-field detector, this may still prove a valuable diagnostic technique for calibration runs. For this reason, some timing properties were implemented in the scintillation model: a single-exponential decay is assumed, with time constants of 26 ns for electrons and 16 ns for recoils.

It should be pointed out that the scintillation and ionisation signals are correlated event-by-event, since recombination will contribute to either one or the other [30]. This correlation has not been taken into account in this model. However, it can improve the discrimination ability of two-phase detectors [12].

2.5 The secondary signal

Under the strong electric field, ionisation electrons are extracted from the interaction site and drifted upward to the liquid surface; once emitted into the gas phase they acquire enough energy to generate many VUV photons by electroluminescence. The S2 signal is proportional to the number of charge carriers extracted from the liquid, as well as the electric field and path length in the gas.

The number of electrons escaping recombination near the interaction site in LXe is calculated according to the electric field strength, the type of interacting particle and its energy. An energy E_d deposited in the liquid creates E_d/W free carriers, where W is the mean energy required to create an electron-ion pair at infinite field. For γ-like interactions, we adopted W_e=15.6 eV [31]. Some of the ionisation produced will recombine at finite field – this fraction depending on the γ-ray energy. Note that our present understanding of charge recombination is not accurate enough to constitute a microscopic model; for this reason, the dependence on particle energy (as opposed to energy deposited in LXe) is the only link to experimental data. We define a fractional charge yield, N_e, representing the number of carriers that escape recombination, as:

$$\frac{1}{N_e} = \left(\frac{30}{E_\gamma} + 0.4\right)\frac{1}{E} + 1.0, \tag{1}$$

where E_γ is the γ-ray energy in keV and E is the field strength in kV/cm [11]. This function parameterises experimental data found in Ref. [32] and is plotted in Fig. 4 a) for the photon energies considered in that study.

The ionisation yield for nuclear recoils was unknown at the start of this work, but it was thought to be much smaller than that for electron recoils. It was reasoned that, to first approximation, the number of ionisations and that of excitations producing scintillation would be suppressed by a similar amount, i.e. W_n=W_e/QF$\simeq$71 eV. Under a finite electric field, only a fraction of this ionisation can be extracted from the nuclear track. Establishing a parallel with α-particle ionisation yields, we adopted a linear dependence with field giving 10% charge yield at 10 kV/cm. Combining these two figures, we predicted that ZEPLIN-III should produce some 40 electrons from a 30 keV nuclear recoil (1.3 e$^-$/keVnr). Recent measurements suggest that nuclear-recoil ionisation may not be a linear function of either recoil energy or electric field, and could be 3–4 times higher than anticipated at 30 keVnr at half the maximum ZEPLIN III field [33]. In view of this, some simulations were repeated with a yield 4 times higher than the default value (5.2 e$^-$/keVnr), but still proportional to recoil energy and field.

The charge carriers released from each interaction site are tracked in the electric field until reaching either the liquid surface or a side-electrode. The drift speed in the liquid has been parameterised from experimental data [34], as shown in Fig. 4 b). The high-field saturation value is $\simeq$3 mm/μs. Neither charge trapping by impurities nor carrier diffusion are considered at this stage in the simulation. For a diffusivity $D\sim$50 cm^2/s [35], one can estimate that the charge arrival times at the liquid surface will be smeared by 0.1 μs following a 10 μs drift. Although this effect is not negligible when compared to the width of S2 itself, it can be taken into account at a later stage.
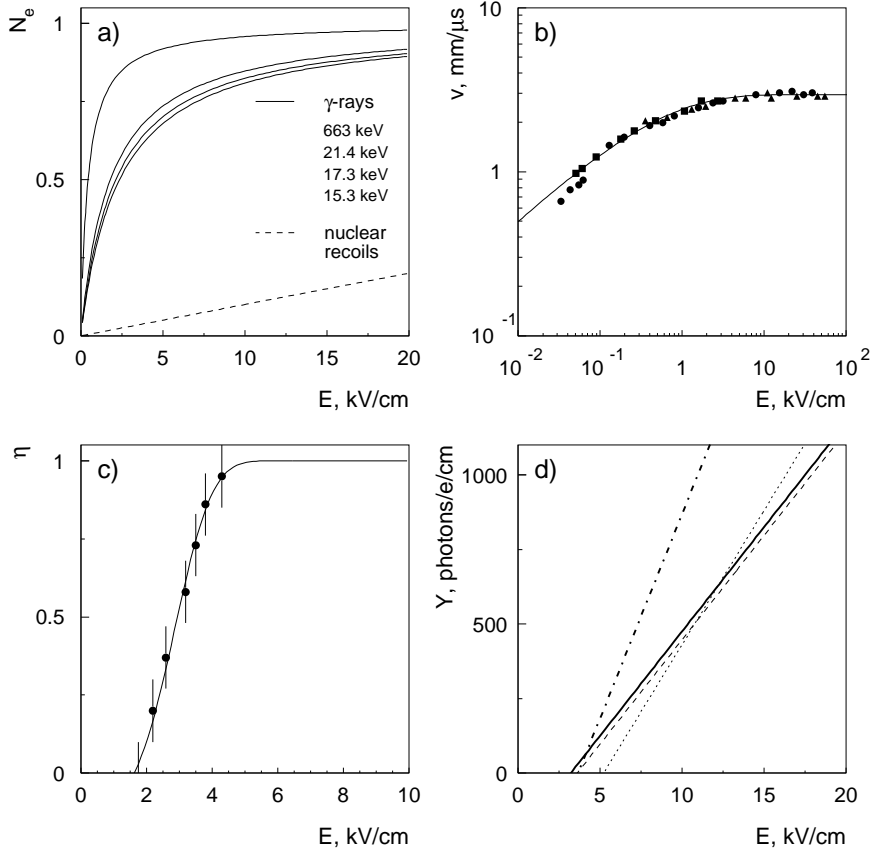
Fig. 4. Electric-field dependence of S2 parameters: a) Relative ionisation yield adopted for γ-rays and nuclear recoils in LXe; γ-ray curves are parameterised from experimental data from Ref. [32] (ordered as in legend). b) Drift speed in LXe, parameterised from data found in Ref. [34]. c) Electron emission probability at liquid/gas interface, parameterised from experimental data in Ref. [36]. d) Electroluminescence yields for gaseous xenon at 4 bar equivalent pressure at 0°C; continuous line: $Y = 70E - 56P_{eq}$ [38]; dashed line: $Y = 70E - 63P_{eq}$ [39]; dotted line: $Y = 90E - 117P_{eq}$ [40]; dash-dotted line: saturated vapour, $Y = 137E - 125P_{eq}$ [41].

Upon reaching the surface, the normal component of the electric field in the liquid determines the fraction η of charge emitted into the gas phase. Experimental data [36] has been parameterised as shown in Fig. 4 c). The ionisation is then tracked in the gas field, generating electroluminescence photons along the way. A reduced drift speed of 1.5 mm/μs/(V/cm/torr) is considered, obtained by extrapolating data in Ref. [37] to high fields.

The electroluminescence yield, defined as the number of VUV photons created per extracted carrier and per cm of track, is calculated according to $Y = 70E - 56P_{eq}$, where E is the field in kV/cm and P_{eq} is the equivalent pressure in bar for the same gas density at 0°C [38]. For a vapour pressure of 2.5 bar ($P_{eq} = 4$ bar) and a nominal field of 17.8 kV/cm, a single electron extracted can

11

produce ~500 photons over a 5 mm gas layer. This and similar yield equations, also shown in Fig. 4 d), have been found for room-temperature gaseous xenon. Recently, photon yields measured with saturated xenon vapour in equilibrium with the liquid phase were shown to be higher than those observed in the warm gas (the latter being consistent with previous experiments) [41]. This brings the prospect of even higher gain in the S2 channel.

The energy resolution achievable in S2 is dominated by fluctuations of the number of ionisation electrons extracted from the track, with lesser contributions from the ensuing stages (emission into the gas, electroluminescence and photon detection). It has long been acknowledged that the intrinsic resolution achievable by charge readout in LXe is worse than both the calculated Fano factor (F=0.04, [35]) and the Poisson limit (F=1) – see e.g. [30]. This has been attributed to the (small-number) statistics of δ-ray production acting together with charge recombination, which can persist even under electric fields as high as 20 kV/cm [42]. This effect is likely to be less marked for energies up to a few tens of keVee. Although most results presented here are for unity Fano factor, F=0 and F=10 were also considered. Further (Gaussian) deviates are applied at the photon generation stage to smear the number of photons produced per electron extracted.

2.6 DAQ Model

In each event optical tracking ends with the probabilistic detection of photons arriving at each PMT photocathode. The phe creation times are then histogrammed into long timelines with 2 ns binning. Two such timelines of the sum of all 31 channels are shown in Fig. 5 for 10 keVee electron and nuclear recoils (15 keVnr) interacting 5 mm below the liquid surface.[2] The two S2 signals differ by a factor of 10 in area for a similar S1 ($\simeq$10 phe, just visible at 2000 ns).

To obtain the PMT output voltage, the impulse response function (i.e. single phe response) is calculated analytically [43] and numerically convolved with the phe timeline [44]. For a gain of 2×10^5, the mean single phe height is 0.16 mV and the pulse area is 1.6 pVs. Such low gain should avoid saturation effects following very large S2 signals. Wideband amplifiers add further gain ($\times$50) and noise (30 μVrms at input) to the signal. Finally, the voltage is digitised with 8-bit resolution. The dual-range DAQ records two traces per channel at 100$\times$ full-scale difference. Fig. 5 c)–f) shows how the summed timeline would appear on both (note that noise from a single channel is considered).

---

[2] Note that keVee is defined as the equivalent (visible) energy for electrons taking into account the field-induced suppression of S1, so keVee=(QF/0.3)keVnr $\simeq$2/3 keVnr.
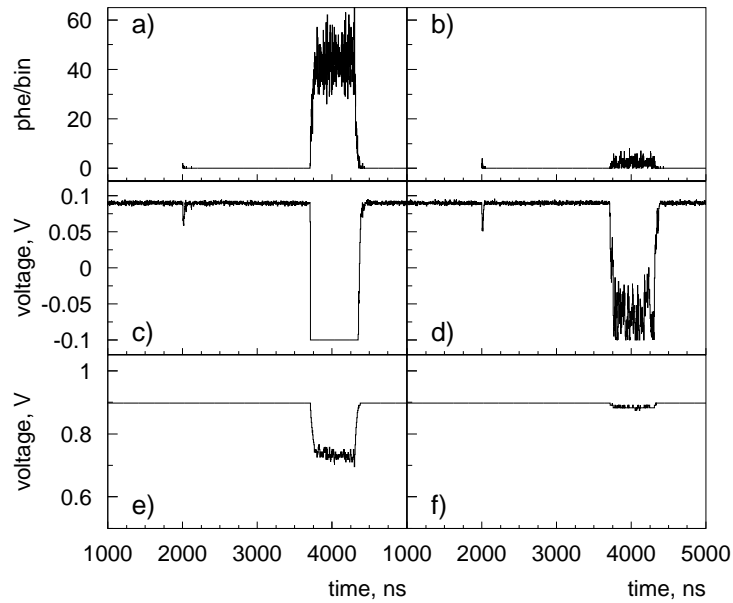
Fig. 5. Simulated timelines (31-channel sum) for 10 keVee electron (left) and nuclear recoil interactions (right). a) and b) are photoelectron timelines; c) and d) show the high-sensitivity DAQ channel; e) and f) show the low-sensitivity DAQ channel.

3 Simulation results

3.1 Simulations of optical response

The optical sensitivity to S1 and S2 are key parameters which affect the detector performance at many levels. The primary scintillation yield across the chamber is shown in Fig. 6 (left) for the default parameters (5 mm of gas, 34.6 cm LXe absorption length, 15% copper reflectivity). It assumes a zero-field scintillation yield of 60 photons/keV in both phases. The light collection is quite uniform across the active LXe region; a reference value for the centre of the target is 3.4 phe/keV at zero field (1.0 phe/keV at maximum field for electron recoils).

Increasing the mirror reflectivity to $R=90\%$ would improve the zero-field value to 4.2 phe/keV. This relatively modest increase is due to the fact that most scintillation photons are internally reflected by the liquid/gas interface and not by the top electrode (and many that do reach the top plate are externally reflected at the liquid surface and remain trapped in the gas phase). Filling the detector to immerse the top mirror decreases the yield from 3.4 phe/keV to 2.3 phe/keV. Increasing the LXe absorption length to a more realistic 100 cm improves the reference yield to 4.0 phe/keV with low-R mirrors.
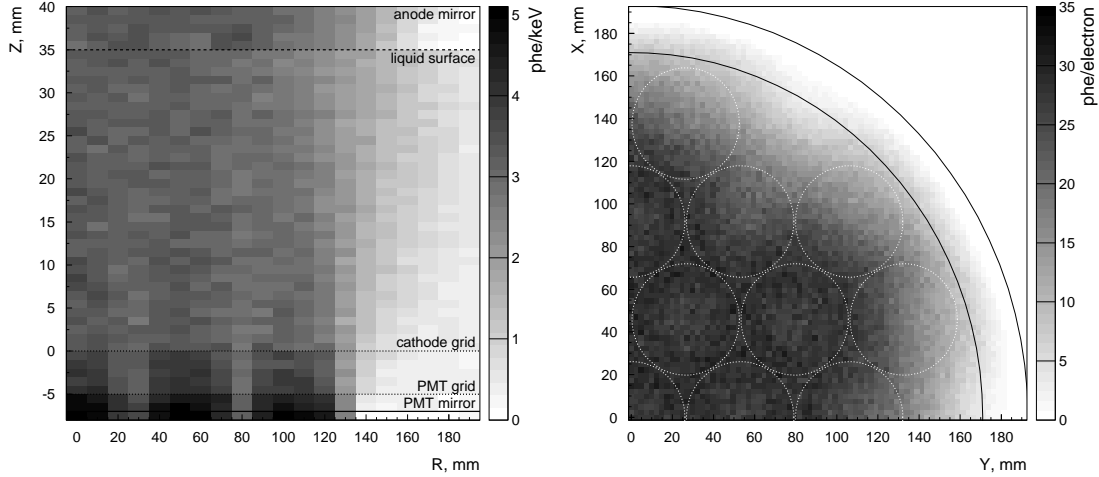
13

Fig. 6. Left: light yield from primary scintillation (S1) with no electric field. Right: light yield from electroluminescence at nominal field.

The S2 light yield was simulated by generating a constant charge over a square grid located under the liquid surface, which is extracted to the gas phase where it generates a varying number of photons – thus taking into account the position-dependent electric field. The result is shown in Fig. 6 (right). The two concentric lines represent the cathode grid and active volume radii. The light collection is quite uniform across the central part of the chamber, where an average 26 phe are generated per electron extracted. Fig. 7 shows the S2 distribution for one and two electrons emitted into the gas. Two populations can be clearly seen when outlying events are cut (>156 mm radius), confirming the sensitivity to single electrons extracted from the target.
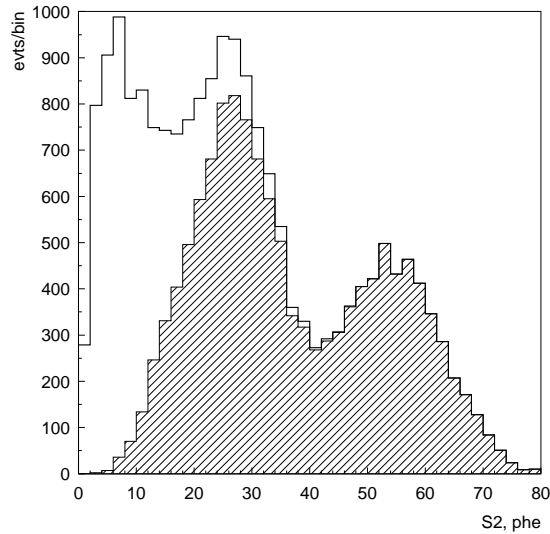

Fig. 7. S2 spectrum for one and two ionisation electrons extracted from the liquid. The shaded distribution includes only events in the inner 8 kg (156 mm).

14

3.2 Position reconstruction

In ZEPLIN-III a fiducial region can be identified in the target without physical boundaries by reconstructing the three coordinates of the interaction. Spatial sensitivity is important in low-background detectors since surface contamination is a source of low-energy events (e.g. nuclear recoils from α decay). Interactions occurring in regions where the electric field and the light collection are not uniform should also be excluded.

In two-phase detectors the z coordinate is obtained with sub-mm precision by the drift time in LXe, as given by the time separation between S1 and S2. The horizontal (x,y) position is reconstructed using a template method; this is outlined here and described in detail elsewhere [45,11]. An analytical method was also shown to be viable [46].

A template was generated by full optical simulation of the S2 response produced from 20000 locations in the gas phase, organised in a square mesh with 2.5 mm pitch. From each point 1.5×10^6 photons were released and tracked, and the signals produced in each PMT were stored to form a template with 20000×31 entries. After simulation of a realistic event, S2 distributions are compared with the stored template responses, and the point with the lowest χ^2 is retrieved as the best estimate of (x,y).

An important requirement of the algorithm is that it should be able to run on-line during data acquisition. Although the event rate expected underground is only a few events/s, it will be higher during surface tests and calibration runs, easily reaching the hardware limit of 100 events/s. To improve the performance of the algorithm, only a sub-set of the template is searched in each event. This population should represent the entire template and must therefore have homogeneous space coverage. This was achieved by selecting the sub-set using a 2-dimensional Sobol sequence – one of a family of so-called 'quasi-random' sequences designed to cover a given interval homogeneously [44]. A faster local search is then performed in the vicinity of the selected point. A 2500-point sub-set proved to be the limit where the resolution is not affected. This allows the algorithm to achieve a reconstruction frequency >200 Hz (on a 3 GHz CPU), which is significantly faster than the maximum DAQ rate.

Random events with 1, 4 and 10 ionisation electrons extracted from the liquid were simulated and their (x,y) coordinates reconstructed, showing resolutions of $\simeq$10 mm (FWHM) for extremely small energy deposits (1 electron) and a few millimetres near the threshold energy (10 electrons). Fig. 8 shows the reconstructed radius for random interactions across the whole active region for 10 electrons extracted, subject to S2>10 phe (this cut eliminates fringe events with low S2 values due to poor light collection and weaker field).
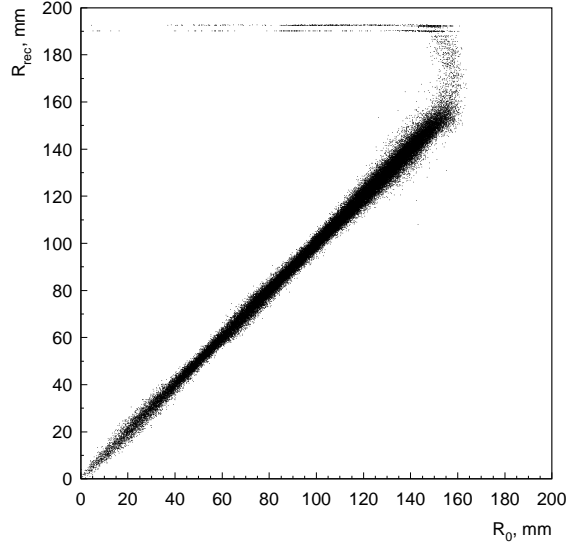
Fig. 8. Plot of the reconstructed radius R_{rec} as a function of the real radius R_0 of the interaction for the whole detector for 10 electrons extracted from the liquid.

Ultimately, the merit of the algorithm must be judged by the size and quality of the fiducial volume that can be derived. Outlying events, with distorted signals, can be placed nearer the centre by the routine and misinterpreted as interesting events. Contamination from these events was studied for several test volumes, showing negligible cross-boundary migration for up to 8 kg (156 mm radius) at very small energy deposits (S2<100 phe). This is a significant improvement over the initial design goal of 5–6 kg.

3.3   Calibration

Calibrating the S1 and S2 channels with electron recoils of suitably low energies throughout the detector volume is not a trivial task. With increasing target masses, calibration with reference to a single point or small region may prove inaccurate. S1 and S2 depend on local electric fields and optical properties which may differ between the LXe bulk and near electrodes and reflectors.

In ZEPLIN-III the γ calibration strategy will consist of: i) a relatively low-energy calibration with ^{57}Co γ-rays for light/charge yield measurements and long-term monitoring of the detector stability; ii) calibration with high-energy γ-rays from ^{60}Co in order to populate near-threshold energies with low-energy Compton electrons; c) low-energy γs from inelastic neutron scattering and from the radioactive decay of xenon and copper radioisotopes produced by neutron activation, which can be used to check the volume uniformity (e.g. inelastic scattering of neutrons emitted by the PMTs cause one such feature seen at 40 keV in Fig. 13 in the following section).
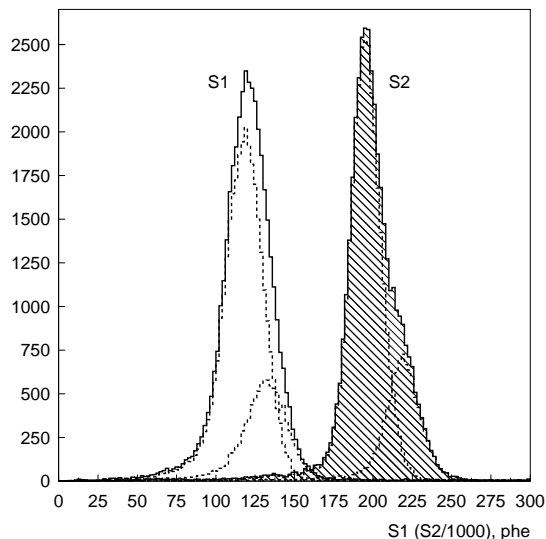
16

Fig. 9. S1 and S2 energy spectra in the inner 8 kg from collimated ^{57}Co source located above the detector. S2 (shaded) is scaled down by a factor of 1000. The contribution of the individual γ energies (122.1 keV and 136.5 keV) is also shown.

We outline here the simulation results for a collimated ^{57}Co source placed above the vacuum vessel, with reference to Fig. 9. In spite of over 1 cm of intervening copper, a reasonable number of 122.1 keV and 136.5 keV photons get through to the target (14 keV γ-rays are completely absorbed). Low-intensity lines at higher energies provide additional calibration points, most notably the 692 keV γ-ray (not shown). The S1 energy resolution for the 122 keV line is 25% (FWHM), close to the value expected from phe statistics. The energy resolution in S2 is slightly better, being mainly determined by the Fano factor at these energies: FWHM$\simeq$12% for F=1. The limiting cases are 9% (F=0) and 15% (F=10) – comparable to the 11% energy separation between the two lines.

Calibration of the response to nuclear recoils will rely on irradiation with an Am-Be (α,n) source in conjunction with independent measurements of the scintillation QF to establish the energy scale. To calculate the recoil spectrum and the required exposure, a 0.1 GBq Am-Be source placed above the outer vessel was simulated. The input neutron spectrum used was that reported in Ref. [47], with no consideration given to γ-rays from the source. The resulting spectrum for single elastic scatters is similar in shape to that obtained for background neutrons from the PMTs which is shown in Fig. 13. Some ~50,000 events/hour are expected above 10 keVnr in the 8 kg fiducial volume, with single scatters constituting approximately 60% of all recoil events.

Activation of xenon and other materials has also been studied and found not to constitute a problem except for unreasonably large exposures. Low energy signals are expected from ^{125}I x- and γ-rays (EC, T$_{1/2}$=59.4 days), which

17

follows from neutron capture on ^{124}Xe. Other Xe isotopes and their metastable states contribute low-energy γs which persist for several days after irradiation, namely ^{129}Xe, ^{131}Xe and ^{133}Xe. Neutron capture on copper is important but mainly during the exposure, since the products are short-lived. Small amounts of ^{55}Fe will be created at the electrode grids, but these low-energy photons can be cut from the data by drift-time.

3.4 Discrimination Power

Low-energy electrons and Xe nuclei (5×10^5) were generated randomly throughout the active volume with a constant energy spectrum. Datasets were produced with: a) ionisation Fano factors $F=0$, 1 and 10 and b) nuclear-recoil ionisation yields proportional to both electric field strength and recoil energy generating an average 12.5 and 50 electrons at 10 keVnr (the two scenarios described in Section 2.5). The number of S1 and S2 phe in each PMT was obtained with full optical tracking. The plot in Fig. 10 shows the ratio S2/S1 for the electron- and nuclear-recoil populations as a function of energy ($\propto$ S1) for $F=1$ and the lower ionisation yield. Interactions outside the 8 kg fiducial region were rejected.

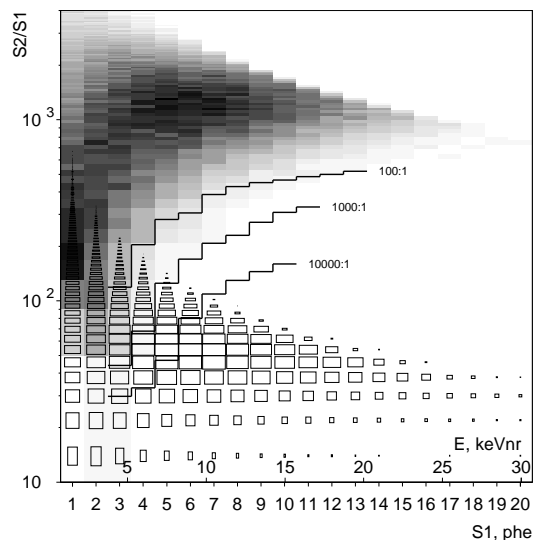

Fig. 10. S2/S1 distributions for electrons (upper population) and nuclear recoils (lower population) in the inner 8 kg, with lower ionisation yield and unity Fano factor. The thick lines represent the boundaries for a given γ-ray discrimination efficiency. The energy axis considers $QF=0.2$.

The lines along the tail of the upper population mark γ rejection efficiencies of 10^n:1 – indicating the S2/S1 ratio at which one event leaks to the nuclear recoil population for every 10^n electron recoils. Higher rejection efficiency boundaries could not be calculated since they would require an unreasonably long simula-

tion. Fig. 11 plots the recoil detection efficiencies obtained with this procedure. In conclusion, 10^4:1 discrimination to γ-rays can be reached between 8 keVnr and 14 keVnr for $F=1$. The combination of high ionisation yield and $F=10$ (not shown) produces a less competitive result.
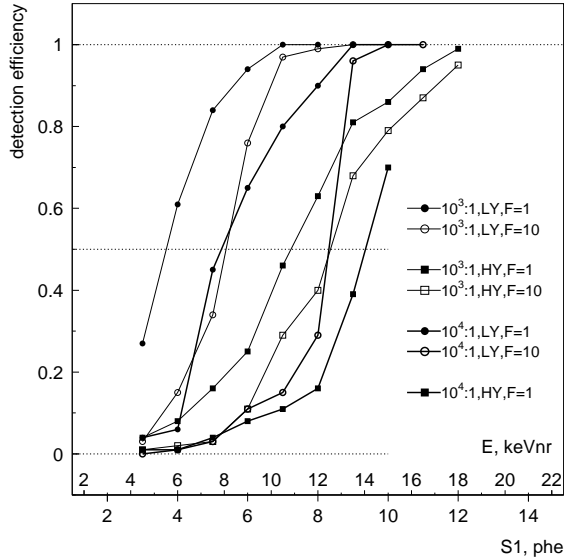

Fig. 11. Nuclear recoil detection efficiency curves for 10^3:1 and 10^4:1 γ discrimination for lower (LY, thin lines) and higher (HY, thick lines) ionisation yields.

One particular class of problematic event requires consideration: γ-rays hitting both the active region and the 'dead' volume below the cathode will produce lower S2/S1 ratios than single interactions in the active volume, since individual S1 signals will add up but only one S2 is generated. The discrimination efficiency will therefore be lower for these events. Simulation of background γ-rays emitted by the PMTs (the dominant source of electron recoils) indicates $\sim$2700 of these multiple scatters per day. The vast majority can be rejected by restricting the S2 location to the fiducial volume ($<$156 mm radius) and requiring that the energy deposits in either regions be below 10 keVee (at higher energies they can easily be discriminated). Ten or so events per day survive these cuts. Of these, the most dangerous ones deposit a small energy in the target (small S2) and a comparatively large energy in the dead region (large S1). Many such cases can be identified by analysing the S1 spatial distribution across the array: a more localised interaction (with many phe in a single channel) is expected relative to a similar amplitude S1 in the active region. This analysis can be extended to take into account that the S1 location should be consistent with the (x,y) point reconstructed from S2. Very few events per day are expected to escape these cuts, and a modest discrimination efficiency (10$\times$ lower than that achieved in the fiducial region) should reduce those to an insignificant contribution.

3.5   Detector Sensitivity

The performance of ZEPLIN-III as a dark matter detector relies ultimately on the number of background events producing signatures which cannot be distinguished from those of WIMPs. Neutrons are the obvious irreducible source of background, but electron recoils which evade discrimination must also be considered. In addition, electron recoils dominate the detector trigger rate, and this has implications for the DAQ operation. In this section we calculate the two types of background from dominant internal and external sources by tracking background particles and looking for energy deposits in the target. Full optical tracking is not performed since the very large dynamic range of the background signals would make this computation overwhelming.

3.5.1   Electron-recoil backgrounds

Trace radioactivity in the PMTs is the major source of background of both γ-rays and neutrons – and consequently the rate of interactions and total energy (light) deposited in active region. The PMT contamination levels were measured at 250 ppb in ^{238}U, 290 ppb in ^{232}Th and 1350 ppm in ^{40}K. γ-rays from ^{40}K plus the secular equilibrium spectra for the ^{238}U and ^{232}Th chains [48] were generated uniformly from the PMT glass and fully tracked until they were absorbed or left the outer vacuum vessel (although the radioactivity is concentrated mainly at the graded seal near the PMT windows and the glass bases, this approximation is not unreasonable). Note that GEANT4 can generate the γ spectrum for the full U and Th chains, in good agreement to the one used here, and producing in addition the correct average number of α, β and γ-rays per parent decay. Low-energy x-rays, α and β radiation interacting very close to the PMT bodies are unlikely to trigger more than one PMT due to the copper screens in which they are located, and for this reason were not considered.

The differential energy spectrum in the target is depicted in Fig. 12 (traces A and B). We predict a low-energy rate of 10 dru (1 dru=1 evt/kg/day/keVee), confirming earlier results [11]. An interaction rate of 5 Bq will be caused above the PMT windows (S1 trigger rate), decreasing to 2.5 Bq above the cathode grid (S2 trigger rate). This corresponds to an average rate of energy deposited just under 2 MeV/s.

A second internal source of electron recoils is the β decay of ^{85}Kr (T$_{1/2}$=10 yr) contaminating the Xe itself. Extracted from the atmosphere in the mid 1960s, the ZEPLIN-III xenon has a low Kr content, estimated at $\sim$5 ppb. The (Coulomb-corrected) β^{-} energy spectrum generated by GEANT4 is tracked in the target, leading to 0.1 dru at low energies (trace D in Fig. 12).
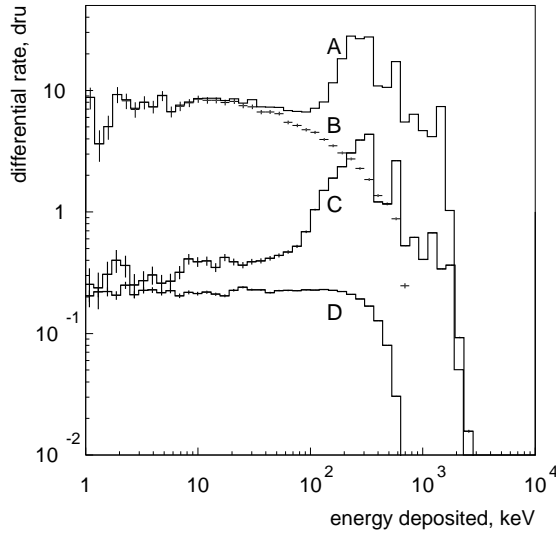
Fig. 12. Electron-recoil background rates. A: Total energy deposit in the active region from PMT γ-rays; B: Same as A, but for single interactions; C: γ-rays from 10 Bq/m^3 of ^{222}Rn progeny (^{214}Bi+^{214}Pb) decaying in air inside the lead shielding; D) Background from β^- decay of ^{85}Kr (5 ppb Kr) in the active volume.

The presence of ^{222}Rn and its progeny in the air surrounding the detector is a source of radioactive background – mainly due short-lived γ-emitters ^{214}Bi and ^{214}Pb. In Ref. [49] an upper limit is placed on the differential rate expected from these isotopes in a large Xe detector surrounded by air contaminated with 10 Bq/m^3 in ^{222}Rn; the result in reproduced in Fig. 12 C. We note that the actual contribution from these isotopes is likely to be even smaller, as both the air volume and contamination level considered are too generous.

Finally, the cavern walls (mainly NaCl) emit γ-rays, requiring extensive lead shielding around the detector. A calculation based on radioactivity measurements of the Boulby rock (67 ppb U, 127 ppb Th, 1300 ppm K) suggests that a lead castle 15 cm thick can attenuate the γ background to <0.01 dru [50].

In conclusion, a total electron-recoil background of 10 dru is expected in a shielded detector, dominated by PMT γ-rays.

3.5.2 Nuclear-recoil backgrounds

Energetic neutrons are produced due to radioactive contamination of detector components and its surroundings with the uranium and thorium decay chains, by spontaneous fission (mainly of ^{238}U) and the (α,n) reaction. Cosmic-ray muons also generate neutrons in spallation reactions and secondary cascades.

Operation deep underground attenuates the muon flux by several decades, but a few neutrons are still produced by muons interacting in the detector ma-

terials and the cavern rock. Muon-induced neutron production at the Boulby Underground Laboratory (2800 mwe) has been studied in the context of a large-scale Xe detector in Refs. [51,52,53]. For the shielding configuration anticipated for ZEPLIN-III one can expect $\lesssim 1$ single nuclear recoil event per year above 10 keVnr in a 8 kg fiducial volume.

The neutron flux in the cavern is instead dominated by U/Th radioactivity in the Boulby rock. The flux at the rock face has been simulated at $\approx 2 \times 10^{-6}$ n/s/cm^2 above 1 MeV (excluding backscattering of reentering neutrons) for the above rock contamination [53,51]. This flux would easily overwhelm an unshielded detector. 20–30 g/cm^2 of hydrocarbon shielding located inside the lead castle should attenuate the neutron flux to acceptable levels – producing fewer than ~ 1 nuclear recoil per year for a complete (4π) shield.

Neutrons produced inside the detector shielding can only be avoided by construction with low-background materials and the use of an active veto surrounding the detector, to record neutrons in coincidence with the target. Construction from mainly high-purity copper (U/Th levels <1 ppb) and the relatively high threshold for (α,n) in Cu ensure a very low neutron background from the vicinity of the target from most components, with the notable exception of the PMTs.
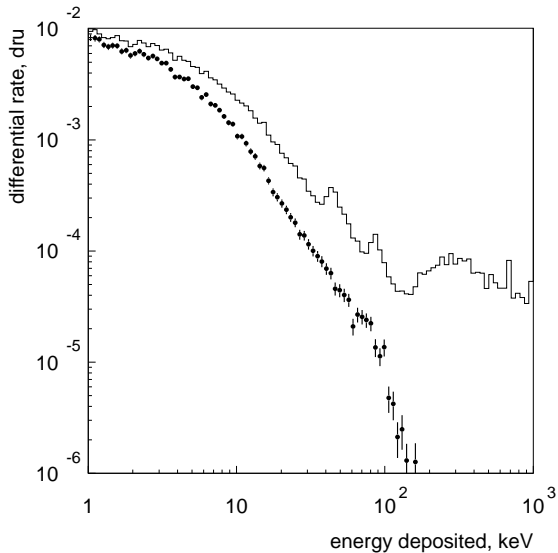

Fig. 13. Differential energy spectrum (evt/kg/day/keVee) from PMT neutrons. The line represents total energy deposited in the target (electron and nuclear recoils), whilst the markers show single nuclear recoils only (in the latter case, the abscissa corresponds to keVnr).

Neutron spectra from fission and (α,n) reactions in the PMT borosilicate glass were calculated using the SOURCES-4A code [54] modified in the way described in Ref. [51], for the U/Th contamination levels mentioned previously. Fig. 13 shows the differential energy spectrum caused in the target by PMT

neutrons emitted isotropically and uniformly from the PMT glass. The figure represents the total energy deposited (elastic plus inelastic events) in addition to single nuclear-recoil events. PMT neutrons reach $\sim 10^{-3}$ dru (e.e.) at low energies, typically contributing 25 events/year above 10 keVnr in the 8 kg fiducial mass.

3.5.3 WIMP sensitivity

Background from the 31 PMTs dominates in a shielded ZEPLIN-III by a large margin. Some 20–40 events/year will be due to neutrons (depending on the energy acceptance considered). In addition, although most γ-rays can be removed by $S2/S1$ discrimination, some will 'leak' into the nuclear recoil population for any realistic discrimination cut adopted. Increasing the latter (e.g. from 10^3:1 to 10^4:1) also raises the energy threshold, as illustrated in Figs. 11 (fortunately, it also decreases the number of neutron events).

The yearly neutron and γ rates are presented in Table 1 for the ionisation yields mentioned previously (1.3 and 5.2 e^-/keVnr) and $F=1$. We adopt a 50% energy threshold, E_0, from the efficiency curves in Fig. 11. The neutron distribution (Fig.13) is integrated above E_0. The number of γ-rays is obtained by integrating a constant rate of 10 dru (Fig. 12) over 2 keVee (very few non-discriminated γs should remain above E_0+2 keVee). The sensitivity limits for the WIMP-nucleon cross-section (spin-independent interaction) are also shown for the minimum of the sensitivity curve (60 GeV WIMP mass), for an exposure of 240 kg×days (1 month at 100% duty cycle) and 3000 kg×days (1 year). These were calculated as described in Ref. [55].

A limiting sensitivity of $3-4 \times 10^{-8}$ pb can be achieved even in a high ionisation yield scenario. This is due to the fact that the reduced energy acceptance for nuclear recoils affects the neutron background more than the WIMP-induced spectrum at these energies. This sensitivity is similar to the original design prediction, and confirms that ZEPLIN-III can probe deep into the parameter space favoured by SUSY in its original design.

An active veto system installed around the detector can be used to reject events in coincidence with the target. A veto efficiency of 50% can be realistically achieved for internal neutrons. A γ-ray veto efficiency of $\simeq$70% has been deemed possible [11]. A relatively modest factor of 2 in WIMP sensitivity can be gained in this way, assuming the veto itself does not contribute to neutron and γ backgrounds.

A very worthwhile planned upgrade is the replacement of the phototubes with newly-developed low-radioactivity ones. A ten-fold reduction in background (neutrons and γs) can be realistically achieved. This would make PMT neutron rates in the target comparable to external neutron backgrounds, pushing the

Table 1. ZEPLIN III background rates and WIMP sensitivity

	low recoil ionisation yield					high recoil ionisation yield				
	E_0	evt/yr		σ_{min}, pb		E_0	evt/yr		σ_{min}, pb	
	keVnr	n	γ	240 kg×days	3000 kg×days	keVnr	n	γ	240 kg×days	3000 kg×days
10^3:1 γ disc.	5.5	40	60	1.0×10^{-7}	6.7×10^{-8}	11	24	60	1.5×10^{-7}	9.5×10^{-8}
10^4:1 γ disc.	8	31	6	6.9×10^{-8}	3.4×10^{-8}	14	16	6	8.8×10^{-8}	3.6×10^{-8}
Veto installed†	8	16	2	4.7×10^{-8}	1.8×10^{-8}	14	8	2	6.3×10^{-8}	2.1×10^{-8}
PMT upgrade †‡	8	1.6	0.2	2.2×10^{-8}	4.2×10^{-9}	14	0.8	0.2	3.8×10^{-8}	5.6×10^{-9}

† For 10^4:1 γ discrimination efficiency
‡ Including veto

WIMP-nucleon cross-section sensitivity down to $\sim 5 \times 10^{-9}$ pb. With these two upgrades in place ZEPLIN-III would compete favourably with much larger targets and more expensive technologies being considered around the world.

4 Conclusion

The ZEPLIN-III performance as a WIMP detector has been assessed using a fully-featured, realistic simulation tool based on GEANT4. The original sensitivity of a few times 10^{-8} pb is confirmed and many aspects of the detector performance have been predicted in anticipation of tests now being carried out in the laboratory.

Some caution must be exercised in interpreting some of these results, notably the discrimination efficiencies and the sensitivity limits derived from them. It is hard to conceive a simulation model which could accurately characterise the tails of the γ and recoil distributions to better than 1 part in 10^4. However, most parameters were conservatively chosen, and the real performance could actually surpass that predicted in this work. We shall now discuss some of these uncertainties.

The reference light yield is likely to be higher than 3.4 phe/keV: early results from our ZEPLIN-II detector (now operating underground) as well as dedicated tests using ZEPLIN-III during its first commissioning run at Imperial College [56] suggest that both the scintillation yield and the photon absorption length in LXe are higher than considered in this simulation, perhaps due to the outstanding purity levels required for charge drift in these large chambers. This will translate directly into an improvement in energy threshold.

New experimental evidence [33] is pointing to larger ionisation yields from nuclear recoils than originally anticipated, more in line with the high-yield scenario considered here. Significantly, it appears that the WIMP sensitivity is remarkably unaffected, at least in this energy range.

The ionisation Fano factor can affect more the potential of LXe as a WIMP target, and F is not really known for electron and nuclear recoil energies of interest. A combination of a high ionisation yield (~ 5 e$^-$/keVnr) and large Fano factor ($F \sim 10$) could make two-phase xenon detectors less attractive a technology for WIMP searches, but this combination is not likely. In addition, we note that the anti-correlation between S1 and S2, due to the fact that ionisation electrons contribute to either one or the other channel, can be exploited to improve the discrimination efficiency during data analysis.

The new recoil ionisation data also reveal a weak dependence on electric field

above $\sim$1 kV/cm (unlike that indicated in Fig. 4 a). Given that charge extraction from electron recoils is still increasing at that field strength, the advantage of high-field operation may prove very significant. Moreover, it is possible that a higher field may decrease the Fano factor and lead to better discrimination, simply because more charge is extracted from the interaction site.

As it stands, ZEPLIN-III should be able to produce a world-beating sensitivity before rival systems and other technologies. With a further upgrade of the phototubes a very significant gain in sensitivity can be achieved, since these dominate both the neutron and γ-ray backgrounds.

5   Acknowledgements

References

[1] T. J. Sumner (2005), *New Astronomy Reviews* **49**, 277–281.

[2] H. M. Araújo (2005), *Proc. Int. Conf. Dielectric Liquids*, Coimbra, Portugal, IEEE Press (IEEE Cat. 05CH37643), 305.

[3] G. J. Alner *et al.* (2005), *New Astronomy Reviews* **49**, 259–263.

[4] G. J. Alner *et al.* (2005), *Nucl. Instrum. Meth.* **A555**, 173–183.

[5] B. A. Dolgoshein, V. N. Lebedenko & B. U. Rodionov (1970), *JETP Lett.* **11**, 513

[6] T. J. Sumner *et al.* (1999), *Proc. 26th Int. Cosmic Ray Conf.*, **2**, ed. D. Kieda, M. Salamon & B. Dingus, 516.

[7] A. S. Howard *et al.* (2001), *Proc. 3rd Int. Workshop on the Identification of Dark Matter*, ed. N. J. C. Spooner & V. Kudryavtsev, Singapore: World Scientific, 457.

[8] D. Yu Akimov *et al.* (2003), *Proc. 4th Int. Workshop on the Identification of Dark Matter*, ed. N. J. C. Spooner & V. Kudryavtsev, Singapore: World Scientific, 371.

[9] H. Araújo (2003), *ZepIII: A (GEANT4) simulation tool for the ZEPLIN-III detector*, ICL Internal Report.

[10] Geant4 Collaboration (2005), *Nucl. Instrum. Meth.* **A506** 250.

[11] D. Davidge (2003), PhD Thesis, University of London.

[12] J. Dawson (2003), PhD Thesis, University of London.

[13] A. Howard & H. Araújo (2000), *'underground_physics' GEANT4 Advanced Example*

[14] T. J. Sumner *et al.*, in preparation.

[15] V. N. Solovov *et al.* (2004), *Nucl. Instrum. Meth.* **A516**, 462–474.

[16] G. M. Seidel, R. E. Lanou & W. Yao (2002), *Nucl. Instrum. Meth.* **A489**, 189–194.

[17] CRC Handbook of Chemistry & Physics, pp. 12-120

[18] A. Levin & C. Moisan (1996), TRIUMF Preprint TRI-PP-96-64, available from *GEANT4 User's Guide for Application Developers* Section 5.2, at `http://www.cern.ch/geant4`.

[19] H. M. Araújo *et al.* (2004), *Nucl. Instrum. Meth.* **A521**, 407–415.

[20] ANSYS Inc. (`www.ansys.com`)

[21] T. Doke & K. Masuda (1999), *Nucl. Instrum. Meth.* **A420**, 62–80.

[22] V. Chepel, M. I. Lopes & V. Solovov (2005), *Rad. Phys. Chem.* **74**, 160–167.

[23] S. Kubota *et al.* (1979), *Phys. Rev. B* **20(8)**, 3486–96.

[24] A. Hitachi *et al.* (1979), *Phys. Rev. B* **27(9)**, 5279–85.

[25] D. Akimov *et al.* (1979), *Phys. Lett. B* **524**, 245–251.

[26] G. J. Alner *et al.* (2005) *Astroparticle Phys.* **23(5)**, 444–462

[27] V. Chepel *et al.* (2005), Submitted to *Astroparticle Phys.* (ArXiv: physics/0512136)

[28] E. Aprile *et al.* (2005), *Phys. Rev. D* **72**, 072006.

[29] J. Dawson *et al.* (2005), *Nucl. Instrum. Meth.* **A545**, 690–698.

[30] E. Conti *et al.* (2003), *Phys. Rev. B* **68**, 054201.

[31] T. Takahashi *et al.* (1975), *Phys. Rev. A* **12**, 1771.

[32] T. Ya. Voronova *et al.* (1989), *Sov. Phys. Tech. Phys.* **34(7)**, 825–827.

[33] E. Aprile *et al.* (2006), (ArXiv: astro-ph/0601552)

[34] L. S. Miller *et al.* (1968), *Phys. Rev.* **166(3)**, 871–878.

[35] T. Doke (1982), *Nucl. Instrum. Meth.* **196(1)**, 87-96.

[36] E. M. Gushchin *et al.* (1979), *Sov. Phys. JETP.* **49(5)**, 856–858.

[37] F. P. Santos *et al.* (1994), *J. Phys. D: Appl. Phys.* **27**, 42–48.

[38] D. Yu. Akimov *et al.* (1998), *Phys. At. Nuc.* **61(7)**, 1241–44.

[39] A. Parsons *et al.* (1989), *IEEE Trans. Nucl. Sci.* **36(1)**, 931–935.

[40] H. N. Ngoc *et al.* (1979), *Nucl. Instrum. Meth.* **A158**, 128.

[41] A. C. Fonseca *et al.* (2004), *IEEE Trans. Nucl. Sci.*, *in press.*

[42] J. Thomas, D. A. Imel, S. Biller (1988), *Phys. Rev. A* **38**, 5793.

[43] A. G. Wright (2003), *Nucl. Instrum. Meth.* **A504**, 245–249.

[44] W. H. Press *et al.*, *Numerical Recipes in C: The Art of Scientific Computing*, 2nd Ed., Cambridge University Press, 1992.

[45] A. Lindote *et al.* (2005), *Nucl. Instrum. Meth.* **A**, *in press.*

[46] V. A. Ditlov *et al.* (2002) *Proc. 4th Int. Workshop on the Identification of Dark Matter*, ed. N. J. C. Spooner & V. Kudryavtsev, Singapore: World Scientific, 383.

[47] J. W. Marsh *et al.* (1995), *Nucl. Instrum. Meth.* **A366**, 340–348.

[48] UKDMC public server, Radioactivity data from Nuclear Data Sheets to Vol. **64** (1991), `http://hepwww.rl.ac.uk/ukdmc/Radioactivity`

[49] M. J. Carson *et al.* (2005), *Nucl. Instrum. Meth.* **A548**, 418–426.

[50] P. F. Smith (2005), UKDMC internal note.

[51] M. J. Carson *et al.* (2004), *Astroparticle Phys.* **21(6)**, 667–687.

[52] H. M. Araújo, V. A. Kudryavtsev, N. J. C. Spooner & T. J. Sumner (2005), *Nucl. Instrum. Meth.* **A545**, 398–411.

[53] C. Bungau *et al.* (2005), *Astroparticle Phys.* **23(1)**, 97–115.

[54] W. B. Wilson *et al.* 1999, *SOURCES-4A Technical Report 13639-LA*, Los Alamos.

[55] G. J. Alner *et al.* (2005), *Phys. Lett. B* **616**, 17–24.

[56] V. Chepel, C. Thorne *et al.* (2006), in preparation.